




Cite this: *Chem. Sci.*, 2024, 15, 146

All publication charges for this article have been paid for by the Royal Society of Chemistry

Exploring the local solvation structure of redox molecules in a mixed solvent for increasing the Seebeck coefficient of thermocells†

Hiroataka Inoue,^a Hongyao Zhou,^b *^a Hideo Ando,^b ^b Sakuya Nakagawa^b and Teppei Yamada *^a

A thermocell is an emerging alternative to thermoelectric devices and exhibits a high Seebeck coefficient (S_e) due to the large change of solvation entropy associated with redox reactions. Here, the S_e of *p*-chloranil radicals/dianions ($CA^{\cdot-/-2-}$) in acetonitrile was drastically increased from -1.3 to -2.6 mV K⁻¹ by the addition of ethanol, and the increment surpassed the estimation of the classical Born model with continuum solvent media. UV-vis spectroscopy and electrochemical measurements at various mixing ratios of acetonitrile to ethanol revealed that the strong hydrogen bonding between ethanol and oxygen atoms of CA^{2-} forms a 4 : 1 solvent-ion pair, while the ethanol molecules binding to CA^{2-} dissociate upon its oxidation to $CA^{\cdot-}$. The local solvation structures of CA^{2-} are in good agreement with density functional theory. This order-disorder transition of the local solvation structure around the $CA^{\cdot-/-2-}$ ions produces a large entropy change and results in a large S_e value. The tailored solvation structure of redox ions by hydrogen bonding is a versatile method applicable to a variety of redox pairs and solvents, contributing to the development of electrolyte engineering for thermocells.

Received 20th September 2023

Accepted 24th November 2023

DOI: 10.1039/d3sc04955h

rsc.li/chemical-science

Introduction

The recovery of low-grade waste heat, especially in the temperature range below 100 °C, is an important task for realizing an energy-sustainable society.¹ A thermocell is an electrochemical system constructed from a pair of identical electrodes and a liquid electrolyte containing a redox pair. A thermoelectric voltage (ΔV) is generated when a temperature gradient (ΔT) is applied between the two electrodes.² Thermocells have gained increasing attention recently, thanks to the inherently higher Seebeck coefficient (S_e , voltage per unit temperature difference), greater scalability, and lower materials cost compared to solid thermoelectric materials. Thermocells have various applications from self-powered liquid-cooling systems^{3,4} to wearable devices converting body heat into electricity.⁵⁻¹³

The improvement of S_e is always desirable, especially for the utilization of a small temperature difference. Increasing the S_e value of thermocells is a major challenge in improving the output power and thermal efficiency. The S_e value is proportional to the entropy change induced by the redox reaction

(ΔS_{rc}) and can be expressed with the number of electrons mediating the redox reaction (n) and Faraday constant (F):

$$S_e = \frac{\Delta V}{\Delta T} = \frac{\Delta S_{rc}}{nF} \quad (1)$$

The value of ΔS_{rc} is induced by the reorganization entropy of the solvation structure around the redox species in the charge-transfer process.^{2,14} Weaver and Hupp evaluated the ΔS_{rc} of transition metal complexes in various solvents.¹⁴ Based on the experimental results and the Born model, the authors found that the ΔS_{rc} values increase with a larger charge density of the redox pair and smaller acceptor numbers of the solvents. Their theory agreed well with the general observations that a ferri/ferrocyanide redox pair ($Fe(CN)_6^{3-/4-}$)^{15,16}—with its extremely large charge density—shows a large ΔS_{rc} value (-135 J K⁻¹ mol⁻¹) and a large S_e value (-1.4 mV K⁻¹).¹⁷

For improving the ΔS_{rc} values, solvent mixing to decrease the acceptor numbers of the electrolyte was studied previously.^{18,19} Pringle and coworkers showed that an addition of 50 vol% dimethyl sulfoxide (DMSO) in an ionic liquid increased the S_e value of the cobalt(II/III) tris(bipyridyl) redox pair from +1.64 to +1.97 mV K⁻¹.¹⁹ In contrast, mixing of DMSO in water decreased the S_e of $Fe(CN)_6^{3-/4-}$, because of the weakened interaction between water and $Fe(CN)_6^{3-/4-}$.¹⁸ The two opposite effects of mixing DMSO in the ionic liquid or in water indicate that the influence of solvent mixing on the S_e value is unpredictable

^aDepartment of Chemistry, Graduate School of Science, The University of Tokyo, 7-3-1 Hongo, Bunkyo-ku, Tokyo, 113-0033, Japan. E-mail: teppei@chem.s.u-tokyo.ac.jp; hozhou@chem.s.u-tokyo.ac.jp

^bFaculty of Science, Yamagata University, 1-4-12 Kojirakawa-machi, Yamagata, 990-8560, Japan

† Electronic supplementary information (ESI) available. See DOI: <https://doi.org/10.1039/d3sc04955h>



solely by the simple addition rule of the physical properties of the bulk solvents based on the Born model of solvation.

Recently, molecular dynamics (MD) simulation provided detailed information on the local solvation structures of redox-active ions.^{20,21} Sun and coworkers improved the S_e of an aqueous ferrous/ferric ($\text{Fe}^{2+}/\text{Fe}^{3+}$) thermocell in a hydrogel by mixing acetone,²¹ and Yang and coworkers investigated the microscopic solvation structure around $\text{Fe}^{2+}/\text{Fe}^{3+}$ ions.²⁰ The authors revealed that the insertion of one acetone molecule into the solvation shell of Fe^{2+} results in its structural distortion. The authors claimed that the order–disorder transition of the solvation structure upon the redox reaction of Fe^{3+} to Fe^{2+} increases the ΔS_{rc} and the S_e . Furthermore, the hydration structure of the $\text{Fe}^{2+/3+}$ redox pair can be tailored by changing pH and counter anions to increase the ΔS_{rc} and S_e .^{22,23} Tailored local solvation around the redox molecules or ions is the key to increasing the S_e ; however, in a water–organic mixed solvent, the strong hydrogen bonding between the solvent water molecules themselves in the organic media often limits the designability of the solvation structure.

In this work, we focused on designing the local solvation structure of an organic redox molecule in an organic–organic solvent mixture. We used a *p*-chloranil radical anion and

dianion ($\text{CA}^{\cdot-}/\text{CA}^{2-}$, Fig. 1a) as the redox pair, and ethanol (EtOH) as the modifier of their local solvation structure in acetonitrile media. Previously, a positive shift of the electrochemical potential of chloranil was observed when methanol was added in an acetonitrile electrolyte.²⁴ In this study, acetonitrile was selected as the solvent medium because of its high dielectric constant, and ethanol was selected as the additive because of its higher boiling point compared to methanol. CA^{2-} creates an ordered solvation structure with EtOH *via* hydrogen bonding between the negatively charged oxygen atoms of CA^{2-} and the hydroxy group of EtOH (Fig. 1b). When CA^{2-} is oxidized to $\text{CA}^{\cdot-}$, the solvation structure of EtOH is broken because of the decreasing charge density of the $\text{CA}^{\cdot-}$ species. UV-vis spectroscopy and density functional theory (DFT) calculations confirmed that the hydroxy group of EtOH is strongly attracted to the electronegative oxygen atoms of CA^{2-} . In addition, electrochemical measurements showed that EtOH and CA^{2-} form a 4 : 1 solvent–ion pair in the acetonitrile media. The order–disorder transition of the EtOH– CA^{2-} pair increased the ΔS_{rc} by $-160 \text{ J K}^{-1} \text{ mol}^{-1}$ and resulted in the highest S_e of -2.6 mV K^{-1} in the organic–organic mixed solvent system. Our results give a new concept of tailoring the local solvation structure around organic redox molecules, which is potentially applicable to

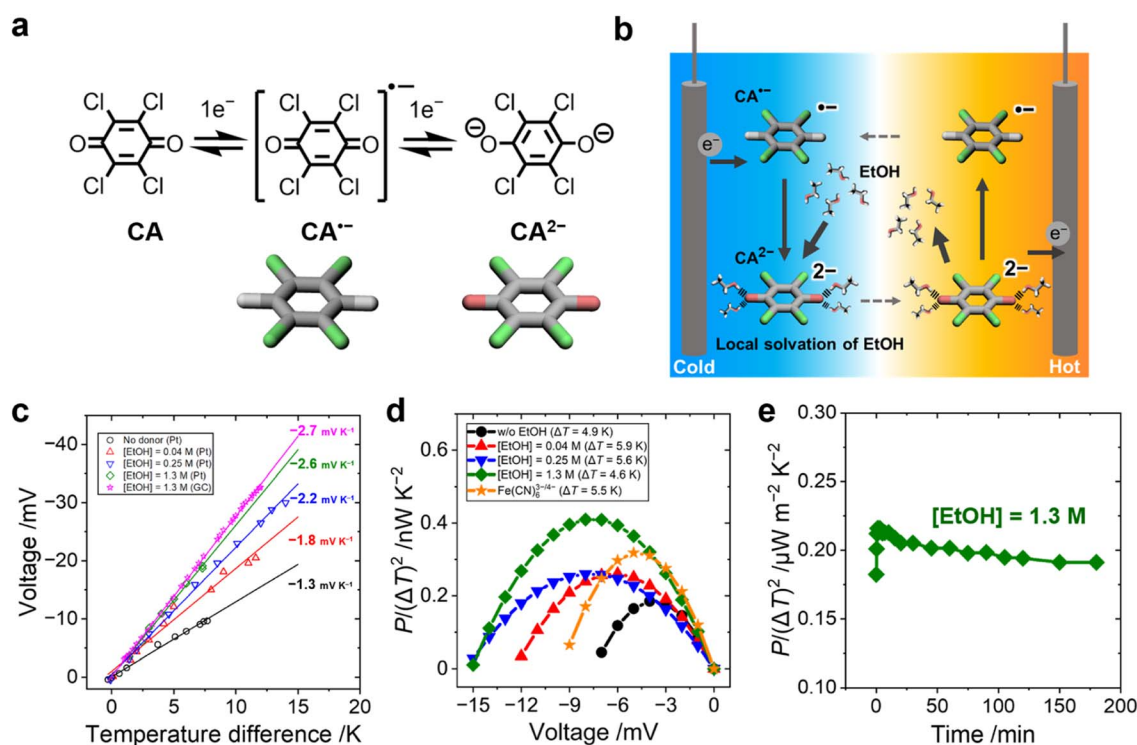


Fig. 1 (a) Two-step one-electron redox reactions of chloranil (CA) and (b) schematics of the $\text{CA}^{\cdot-}/2-$ thermocell. $\text{CA}^{\cdot-}$ is reduced to CA^{2-} on the low-temperature side and forms an ordered solvation structure with EtOH *via* hydrogen bonding. The EtOH dissociates from CA^{2-} after its oxidation to $\text{CA}^{\cdot-}$ on the high-temperature side. This order–disorder transition of the local solvation structure around CA^{2-} produces a large entropy change and a high S_e . (c) Open-circuit voltage *versus* temperature difference across the $\text{CA}^{\cdot-}/\text{CA}^{2-}$ thermocell with various concentrations of EtOH added. The voltage was measured with both platinum (Pt) and glassy carbon (GC) electrodes at $[\text{EtOH}] = 1.3 \text{ M}$. The S_e increases with increasing concentration of EtOH in acetonitrile. (d) Power factor of $\text{CA}^{\cdot-}/2-$ thermocells with the addition of EtOH. The power factor of an aqueous $\text{Fe}(\text{CN})_6^{3-/4-}$ thermocell is shown for comparison. (e) Electrode = Pt. (e) The time-course of the power output of the $\text{CA}^{\cdot-}/\text{CA}^{2-}$ thermocell with 1.3 M EtOH held at $\Delta T = 12\text{--}13 \text{ K}$ and $\Delta V = -16.7 \text{ mV}$. $[\text{CA}^{\cdot-}/2-] = 0.5 \text{ mM}$ and $[\text{TBAPF}_6] = 0.1 \text{ M}$; $[\text{K}_{3/4}\text{Fe}(\text{CN})_6] = 0.5 \text{ mM}$ and $[\text{KCl}] = 0.1 \text{ M}$; electrode = GC.



many other combinations of benzoquinone derivatives and hydrogen bonding donors.

Results and discussion

Thermoelectric conversion by the $CA^{\cdot-}/CA^{2-}$ redox pair in EtOH–acetonitrile mixed solvent

CA undergoes two-step one-electron redox reactions in an organic electrolyte, as shown in Fig. 1a. The S_e value of $CA^{\cdot-/-2-}$ (0.5 mM) in the acetonitrile electrolyte was evaluated with an H-shape glass cell (Fig. S1a and S2b, ESI†). Fig. 1c shows a linear increase of ΔV with increasing ΔT between the two platinum electrodes. The addition of EtOH increased the S_e from -1.3 to -2.6 $mV K^{-1}$ ([EtOH] = 1.3 M) when measured with a Pt electrode. A similar S_e value (-2.7 $mV K^{-1}$) was observed when glassy carbon (GC) was used as the electrode.

The normalized power output, $P/(\Delta T)^2$, of the $CA^{\cdot-/-2-}$ cell was measured with various concentrations of EtOH (Fig. 1d). The result was compared with that of an aqueous electrolyte containing the same concentration of $Fe(CN)_6^{3-/4-}$ (0.5 mM each).^{25,26} The S_e value of $Fe(CN)_6^{3-/4-}$ was -1.6 $mV K^{-1}$ (Fig. S3, ESI†) and agreed with the literature value.²⁷ The $P/(\Delta T)^2$ of the organic $CA^{\cdot-/-2-}$ thermocell surpassed the value of the aqueous $Fe(CN)_6^{3-/4-}$ thermocell when 1.3 M EtOH was added to acetonitrile electrolyte because of the increased S_e value (see Fig. S4, ESI† for the $I-V$ curve). One drawback of the organic $CA^{\cdot-/-2-}$ thermocell is, however, a much lower solubility of $CA^{\cdot-/-2-}$ in acetonitrile compared to the solubility of $Fe(CN)_6^{3-/4-}$ in water. The output power of the $CA^{\cdot-/-2-}$ thermocell could be improved by using quinone derivatives as the redox molecule with a high solubility in organic electrolytes.

Continuous power generation of the $CA^{\cdot-/-2-}$ thermocell with EtOH (1.3 M) was confirmed at a constant voltage load (Fig. 1e). Stable power output for more than three hours was observed without any precipitation. Previously, an addition of 20 wt% methanol (MeOH) in water was reported to increase the S_e of the $Fe(CN)_6^{3-/4-}$ thermocell to -2.9 $mV K^{-1}$.²⁸ The low solubility of $Fe(CN)_6^{3-/4-}$ in MeOH caused precipitation,¹⁸ which increased the S_e values by the concentration gradient of $Fe(CN)_6^{3-/4-}$ between the hot and cold electrodes,^{29–31} while this precipitation can prevent the diffusion of the redox species and deteriorate the output power over time.^{32,33} In this study, no precipitation is caused by the mixing of EtOH, clearly discerning the influence of precipitation and the solvation effect.

Local solvation structure of the CA^{2-} dianion

We investigated the solvation structure of CA species by UV-vis spectroscopy of neutral CA, $CA^{\cdot-}$, and CA^{2-} in acetonitrile electrolyte. We also studied the EtOH solvation structure in the acetonitrile continuum medium and its spectral effects using DFT and time-dependent extension (TD-DFT),³⁴ respectively, along with the B3LYP functional^{35–37} and (aug)-cc-pVDZ basis set.^{38,39} (The details of the DFT-based exhaustive search for EtOH configurations and the TD-DFT calculations are summarized in the ESI†). The calculated (λ_{calc}) and observed (λ_{obs}) UV-vis spectra of the CA species in solvent acetonitrile without EtOH are shown in Fig. S9 and S5 (ESI†), respectively. The absorption peaks of the CA species (Table 1) agree well with literature values.^{24,40}

The UV-vis spectra of the CA species with the addition of EtOH were measured to investigate the effect of EtOH on the electronic states of the CA species. The addition of EtOH caused negligibly small red shifts (by 2 nm at maximum) in the absorption peaks of CA (at 288 nm) and $CA^{\cdot-}$ (at 448 nm) (Fig. S6a and b, ESI†). In contrast, a significantly large blue shift (by 30 nm at maximum) was observed in the absorption peak of CA^{2-} at 359 nm with increasing concentration of EtOH (Fig. 2a (top), Fig. 2b, and S6c, ESI†). The TD-DFT calculations show a similar blue shift (Fig. 2a, bottom) and indicate that the absorption peak at 359 nm (381 nm in theory) is assignable to the electron excitation from a $\pi^*(b_{2g})$ orbital to a $\pi^*(a_u)$ orbital. The $\pi^*(b_{2g})$ one is the highest occupied molecular orbital (HOMO), and the $\pi^*(a_u)$ one is the second lowest unoccupied molecular orbital (LUMO+1) (Fig. 2c). Solvent exchange from acetonitrile to EtOH within the polarizable continuum model (PCM) framework resulted in no peak shift of CA^{2-} (Fig. S9b, ESI†). The change in the dielectric constant of the solvent causes a minimum effect on the electronic structures of the CA species, which highlights the importance of the hydrogen bonding around CA^{2-} .

The calculated molecular geometry of the EtOH– CA^{2-} solvent–ion pair shows that, because of a balance between the hydrogen bonding and the steric jamming among the EtOH molecules, four EtOH molecules are expected to bind with one CA^{2-} ion at maximum (Fig. 2c; the detailed explanation presented in the ESI†). The energy gap between $\pi^*(b_{2g})$ and $\pi^*(a_u)$ (*i.e.*, the HOMO–LUMO+1 gap), as well as the corresponding excitation energy, increases with increasing number of EtOH

Table 1 Assignment of the absorption peaks of UV-vis spectra of $CA^{\cdot-}$ and CA^{2-} ^a

	λ_{calc} (nm)	λ_{obs} (nm)	Peak assignment
$CA^{\cdot-}$	219	214	${}^2B_{3u} \leftarrow {}^2B_{2g} (\pi^*(a_u) \leftarrow \pi(b_{1g}))$
	274	321	${}^2B_{3u} \leftarrow {}^2B_{2g} (\pi^*(b_{3u}) \leftarrow \pi^*(b_{2g}), \pi^*(a_u) \leftarrow \pi(b_{1g}))$
	406	420	${}^2A_u \leftarrow {}^2B_{2g} (\pi^*(a_u) \leftarrow \pi^*(b_{2g}))$
	428	448	${}^2B_{3u} \leftarrow {}^2B_{2g} (\pi^*(b_{2g}) \leftarrow \pi(b_{3u}))$
CA^{2-}	219, 222	223	${}^1B_{1u} \leftarrow {}^1A_g (\pi^*(a_u) \leftarrow \pi(b_{1g}), Rydberg(b_{3u}) \leftarrow \pi^*(b_{2g}))$
	253	258	${}^1B_{1u} \leftarrow {}^1A_g (\pi^*(b_{3u}) \leftarrow \pi^*(b_{2g}))$
	381	359	${}^1B_{2u} \leftarrow {}^1A_g (\pi^*(a_u) \leftarrow \pi^*(b_{2g}))$

^a The λ_{calc} values correspond to the calculated excitation energies in stick spectra (see the ESI for further details, including the molecular orbitals in Fig. S7 and S8).





Fig. 2 (a) Observed and calculated UV-vis spectra of CA²⁻ in acetonitrile without and with the addition of EtOH. The blue shift was observed with increasing EtOH concentration. The calculated oscillator strengths (*f*) of the X ← ¹A_g excitations of CA²⁻ are indicated by the vertical lines, where X is the final electronic state of excitations with *f* > 0.05. (b) Experimental excitation energy shifts (absolute values) of CA⁻ (448 nm) and CA²⁻ (359 nm) at various EtOH concentrations. (c) Calculated ¹B_{2u} ← ¹A_g excitation energies versus the orbital energy gaps between the HOMO and LUMO+1 of CA²⁻ and the *n*EtOH–CA²⁻ solvent–ion pair (*n* = 1, 2, 3, 4). The *n*EtOH–CA²⁻ pair is denoted by CA²⁻(*n*)⋯*n*EtOH. All the energies were calculated at the B3LYP/aug-cc-pVTZ level.

molecules binding with CA²⁻ (Fig. 2c). The electropositive proton of the hydroxy group of EtOH approaches the two electronegative oxygen atoms of CA²⁻, particularly their out-of-plane 2p-type lobes of the π*(b_{2g}) orbital (Fig. 2c), thereby decreasing the π*(b_{2g}) energy level, increasing the HOMO–LUMO+1 gap and causing the blue shift.

Entropy and enthalpy changes upon the association of EtOH with CA²⁻

The entropy (Δ*S*_{as}) and enthalpy (Δ*H*_{as}) changes produced upon the association of EtOH with the CA^{-/2-} redox pair were estimated from the shift of the equilibrium potentials (*E*_{1/2}) with increasing EtOH concentrations and temperatures. Previously, hydrogen bonding between benzoquinone dianions and hydrogen-donating additives—such as alcohols^{24,41–45} and amides⁴⁶—was reported to shift the *E*_{1/2} toward positive potential. In this study, square wave voltammetry (SWV) of CA was performed to evaluate the influence of EtOH on the *E*_{1/2} of each CA species (CA^{0/-/2-}). One peak at -0.25 V was assigned to the redox equilibrium of the CA^{0/-} pair (*E*_{1/2}^I) and the other peak at -1.1 V was assigned to the redox equilibrium of CA^{-/2-} (*E*_{1/2}^{II}) (Fig. 3a). The addition of EtOH drastically shifted the *E*_{1/2}^{II} to a positive potential, which results from the reduced HOMO level caused by the coordination of EtOH to CA²⁻.

The temperature dependence of *E*_{1/2} corresponds to the Δ*S*_{rc} according to eqn (1), and changes in Δ*S*_{rc} caused by the addition of EtOH can be ascribed to the effect of Δ*S*_{as}. The SWV measurement at various temperatures shows that the addition of EtOH drastically enhances the negative shift of *E*_{1/2}^{II} with increasing temperature, indicating that the coordination of EtOH to CA²⁻ increases the Δ*S*_{rc} (Fig. 3b and c). The increment of *E*_{1/2}^I and *E*_{1/2}^{II} versus the EtOH concentration was fitted by using theoretical models based on the Nernst equation, and the binding constant, Δ*H*_{as} and Δ*S*_{as} of EtOH to CA^{-/2-} were

obtained from the fitting parameters (Fig. S18–S20, ESI† the derivation of the theoretical models is shown in the ESI†).

The maximum coordination number of EtOH molecules to one CA²⁻ dianion was set to 4:1 based on the calculated molecular geometry (Fig. 2c). To reduce the number of fitting parameters, only even numbers of EtOH molecules (2 or 4) were allowed to associate with one CA²⁻ in this fitting, which is a reasonable approximation, considering the symmetric structure of CA²⁻. The fitting results of Δ*H*_{as} and Δ*S*_{as} are summarized in Table 2, and the selective association of EtOH to CA²⁻ can be attributed to the larger Δ*H*_{as} with CA²⁻ than with CA⁻. The average number of EtOH molecules associated with one CA⁻ or CA²⁻ anion at each EtOH concentration was calculated from the binding constants, and the result shows that two EtOH molecules associate with one CA²⁻ ion at 0.1 M EtOH, and four EtOH molecules above 1 M EtOH on average, which is larger than the association number of EtOH to CA⁻ (Fig. 3d). This result is consistent with the DFT calculation—EtOH more strongly binds with CA²⁻ than with CA⁻ (Fig. S15 and S16, ESI†).

The Δ*S*_{rc} of the CA^{-/2-} redox pair at various EtOH concentrations was evaluated by temperature-variable SWV measurement (Fig. S21, Table S2, ESI†) and plotted together with the theoretical curve (Fig. 3e; the derivation is shown in the ESI†). Fig. 3e can be divided into three regions: Region 1 shows only a minimum increase of Δ*S*_{rc}, because of little or no association of EtOH with CA²⁻ or CA⁻ ions; Region 2 shows the maximum increase of Δ*S*_{rc}, because the number of EtOH binding with CA²⁻ significantly increases and forms a 4:1 solvent–ion pair at maximum, while the association number with CA⁻ remains low; Region 3 shows decreasing Δ*S*_{rc} values, mainly because the number of EtOH binding with CA⁻ increases at such a high EtOH concentration (Fig. S22, ESI†). The above discussions point out that, in the mixed solvent system, the Born model—



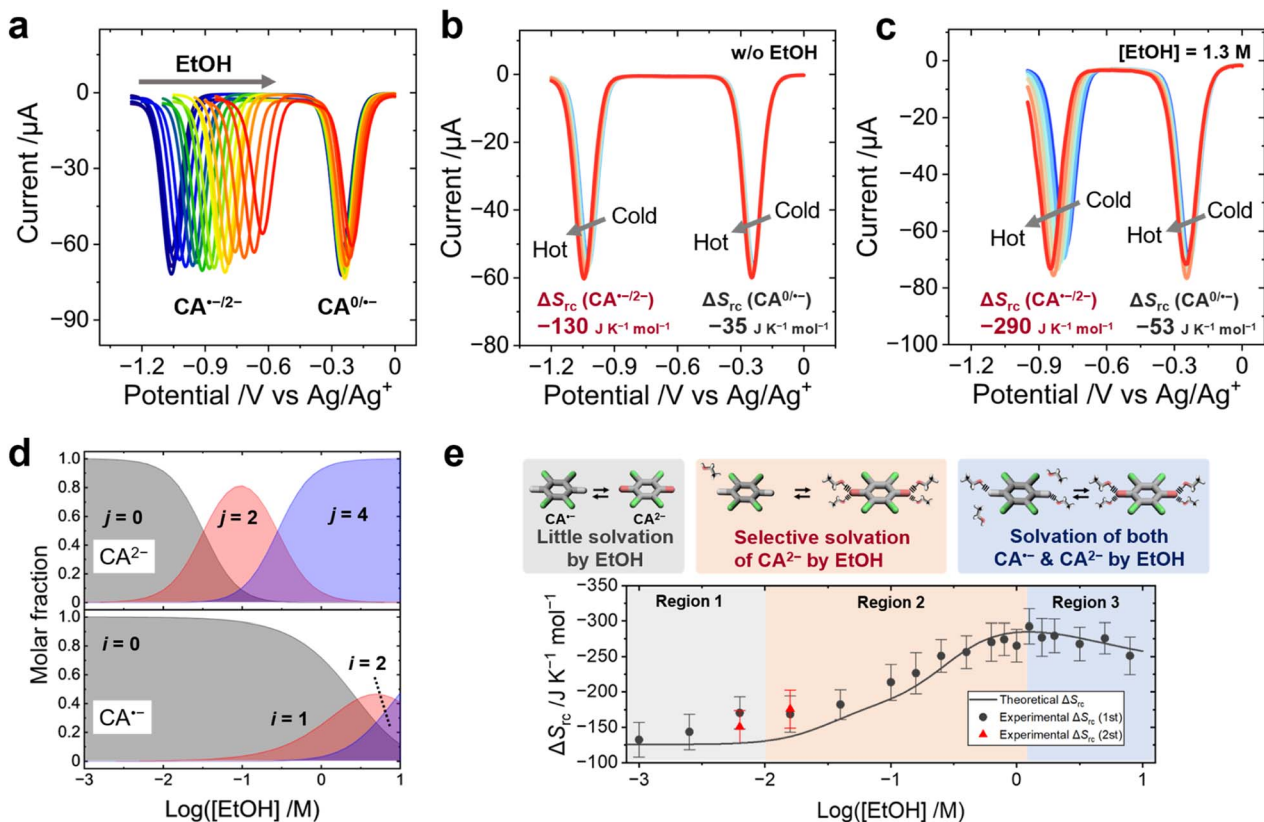


Fig. 3 (a) SWV of CA showing a positive shift of $E_{1/2}$ with increasing concentrations of EtOH at room temperature. (b and c) The SWVs of CA with increasing temperature without (b) or with (c) 1.3 M EtOH. (d) Calculated molar fractions of EtOH molecules binding with $CA^{\bullet-}$ and CA^{2-} at various concentrations of EtOH at 298 K. The symbols, i and j , show the numbers of EtOH molecules binding with $CA^{\bullet-}$ and CA^{2-} , respectively. (e) Experimental values and simulation curves of ΔS_{rc} of the $CA^{\bullet-}/CA^{2-}$ redox pair at various concentrations of EtOH. The ΔS_{rc} values at 0.0063 and 0.016 M EtOH were measured twice. Error bars are the standard deviation of the fitting values of ΔS_{rc} . [CA] = 1.0 mM, [EtOH] = 0–7.9 M, and [TBAPF₆] = 0.1 M.

Table 2 Enthalpy and entropy changes in the association of the corresponding numbers of EtOH molecules bonding with the $CA^{\bullet-}$ radical (i) or CA^{2-} anion (j)

	Number of EtOH	ΔH_{as} (kJ mol ⁻¹)	ΔS_{as} (J K ⁻¹ mol ⁻¹)
$CA^{\bullet-}$	$i = 1$	-9.1 ± 0.2	-39 ± 1
	$i = 2$	-12 ± 0	-66 ± 0
CA^{2-}	$j = 2$	-34 ± 1	-59 ± 3
	$j = 4$	-77 ± 0	-180 ± 1

regarding the solvent as a continuum medium—fails to explain the molecular-level interaction between the redox ions and the solvent molecules. Rather, the molecular dynamics and the intermolecular forces at the microscopic level play a critical role in determining ΔS_{rc} . The slight deviation of the experimental values of ΔS_{rc} from the simulation curve is likely due to the gradual vaporization of EtOH from the electrolyte during the SWV measurement at high temperature (details are discussed in the ESI†).

Supramolecular thermocells developed previously by us exemplify that the molecular-level host-guest interaction can boost the S_e value.^{30,47–49} Briefly, cyclodextrins (CDs) encapsulate the redox-active triiodide anion at the cold electrode and release

the guest triiodide at the hot electrode. This host-guest interaction is driven by the hydrophobic interaction, and the increment of S_e values induced by the addition of CDs is linearly proportional to the entropy change induced by the host-guest encapsulation.²

The CA-based thermocell developed here was inspired by the selective host-guest interaction used in a supramolecular thermocell system. The formation of the 4 : 1 EtOH- CA^{2-} pair produces a ΔS_{as} of -180 J K⁻¹ mol⁻¹, surpassing the largest entropy change obtainable from the host-guest encapsulation between the CD and triiodide (-150 J K⁻¹ mol⁻¹). The order-disorder transition of the solvent-ion pair was found to be a more effective strategy for enhancing the ΔS_{rc} and S_e .

The charge-transfer kinetics of CA^{2-}

The influence of EtOH on the electron-transfer kinetics of $CA^{0/+}$ and $CA^{\bullet-}/CA^{2-}$ redox pairs was studied by electrochemical impedance spectroscopy (EIS) performed at different potentials (-0.277 or -1.085 V vs. Ag/Ag⁺ for studying the charge-transfer process of $CA^{0/+}$ or $CA^{\bullet-}/CA^{2-}$, respectively). One semi-circle was observed in the Nyquist plot of the $CA^{0/+}$ redox pair (Fig. 4a), while two semi-circles were observed in that of the $CA^{\bullet-}/CA^{2-}$ redox pair (Fig. 4b). One of the semi-circles observed in the



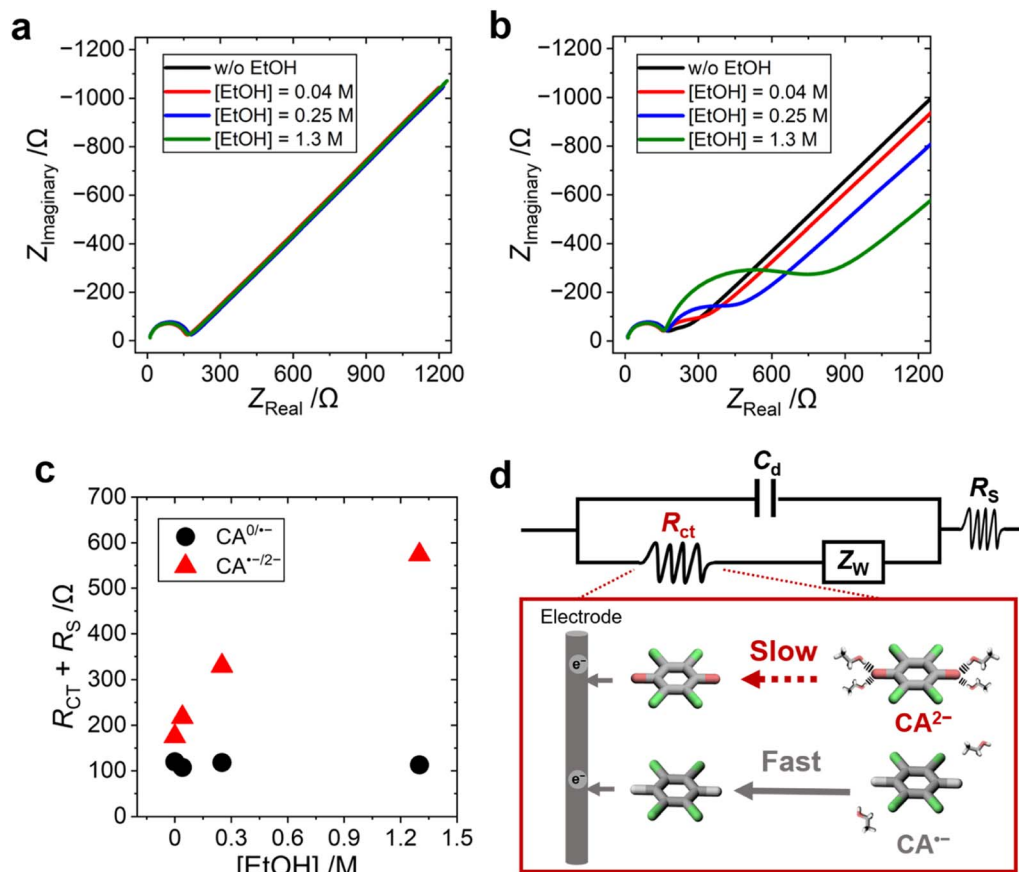


Fig. 4 (a and b) Nyquist plots of (a) CA/CA^{•-} and (b) CA^{•-}/CA²⁻ redox pairs and (c) the sum of the solution resistance (R_s) and charge transfer resistance (R_{ct}) in acetonitrile with various EtOH concentrations. (d) The equivalent circuit and schematics showing the charge-transfer processes of CA^{•-} and CA²⁻ near the electrode surface, and dissociation of EtOH from CA²⁻ increases the R_{ct} . [CA] = 1.0 mM, [TBAPF₆] = 0.1 M, and [EtOH] = 0, 0.040, 0.25, and 1.3 M.

higher-frequency region was attributed to the solution resistance (R_s) and the formation of the electric double layer (C_d), and the other semi-circle observed in the lower-frequency region was attributed to the charge transfer resistance (R_{ct}). The two semicircles are merged in the redox process between CA⁰ and CA^{•-} (Fig. 4a) because of the extremely fast electron-transfer kinetics of the organic radical anion (see Fig. S23, ESI,† for the detailed discussion). The addition of EtOH increased the R_{ct} of the CA^{•-}/CA²⁻ redox pair, while that of the CA^{0/•-} redox pair showed no change (Fig. 4c).

The equivalent circuit diagram and the molecular pictures of the charge-transfer process of the CA^{•-}/CA²⁻ redox pair on the electrode surface are shown in Fig. 4d. The EtOH molecules around CA²⁻ form a strong hydrogen bonding, and the dissociation of EtOH molecules is the rate-determining step in the electron-transfer process from CA²⁻ to the electrode. In contrast, the CA^{•-} radical anion and neutral CA⁰ species form weak or no hydrogen bonding with EtOH solvent molecules, and the electron-transfer process is unhindered between CA⁰ and CA^{•-}. A similar result was previously reported that the reorganization of solvent water molecules influences the kinetics of the Fe(CN)₆^{3-/4-} redox reaction.⁵⁰ The increasing R_{ct} of the CA^{•-}/CA²⁻ redox pair with increasing concentration of EtOH

further supported our hypothesis that the large ΔS_{rc} is caused by the tight hydrogen bonding between the solvent EtOH and CA²⁻ dianion.

Conclusions

The new concept of forming a selective hydrogen bonding between a protic solvent and an organic redox molecule was presented here. The S_e value of CA^{•-}/CA²⁻ in acetonitrile electrolyte was enhanced from -1.3 to -2.6 mV K⁻¹ by mixing 1.3 M EtOH. The S_e value of -2.6 mV K⁻¹ is the highest value among other thermocells based on all-organic electrolytes without introducing the precipitation of the redox species. The organized local solvation structure of EtOH molecules around CA²⁻ was observed from the blue shift in the UV-vis spectra and confirmed by DFT calculations. SWV and EIS measurements supported our concept that the order-disorder transition of the EtOH-binding local solvation structure can significantly increase the entropy change of the redox reaction from CA²⁻ to CA^{•-}. Our concept of using hydrogen bonding to maximize the entropy change of redox reactions is applicable to many other benzoquinone derivatives, organic solvents, and hydrogen-bonding donor solvents and provides a versatile way of



improving the performance of thermocells. Organic thermocells are potentially advantageous in terms of the inherently high boiling point and low thermal conductivity and hold great promise to overperform conventional aqueous thermocells. In addition, our method of exploiting the entropy change of organic redox molecules can give a deeper understanding on the thermodynamics of organic redox-flow batteries. The concept of order-disorder transition of organized local solvation structures can be applied to various electrochemical systems using organic redox molecules.

Data availability

The datasets supporting this article have been uploaded as part of the ESI.†

Author contributions

H. I., H. Z., and T. Y. formulated the original concept; H. I. performed all the experiments; S. N and H. A. performed the theoretical calculations. H. I. analyzed and visualized all the experimental data. H. I. wrote the original draft, and H. Z., H. A., and T. Y. reviewed and edited the manuscript. All authors agree with the final version of the manuscript.

Conflicts of interest

There are no conflicts to declare.

Acknowledgements

This work was supported by JSPS KAKENHI grant numbers: 21H00017 (Hydrogenomics), 20H02714, 21H05870, 20K21176, 21J21893, JST CREST grant number: JPMJCR22O5, The Murata Science Foundation, The Asahi Glass Foundation, Tanikawa Fund Promotion of Thermal Technology, Yamada Science Foundation, The Iwatani Naoji Foundation, and The Canon Foundation. We would like to show our appreciation to Mr Takashi Kobayashi for his experimental support in square wave voltammetry measurements.

Notes and references

- 1 A. Firth, B. Zhang and A. Yang, *Appl. Energy*, 2019, **235**, 1314–1334.
- 2 H. Zhou, H. Inoue, M. Ujita and T. Yamada, *Angew. Chem., Int. Ed.*, 2023, **62**, e202213449.
- 3 Y. Ikeda, Y. Cho and Y. Murakami, *Sustainable Energy Fuels*, 2021, **5**, 5967–5974.
- 4 A. H. Kazim, A. S. Boeshaghi, S. T. Stephens and B. A. Cola, *Sustainable Energy Fuels*, 2017, **1**, 1381–1389.
- 5 Y. Liu, S. Zhang, Y. Zhou, M. A. Buckingham, L. Aldous, P. C. Sherrell, G. G. Wallace, G. Ryder, S. Faisal, D. L. Officer, S. Beirne and J. Chen, *Adv. Energy Mater.*, 2020, **10**, 2002539.
- 6 C. Bai, Z. Wang, S. Yang, X. Cui, X. Li, Y. Yin, M. Zhang, T. Wang, S. Sang and W. Zhang, *ACS Appl. Mater. Interfaces*, 2021, **13**, 37316–37322.
- 7 T. Ding, Y. Zhou, X. Q. Wang, C. Zhang, T. Li, Y. Cheng, W. Lu, J. He and G. W. Ho, *Adv. Energy Mater.*, 2021, **11**, 2102219.
- 8 Y. Zhou, Y. Liu, M. A. Buckingham, S. Zhang, L. Aldous, S. Beirne, G. Wallace and J. Chen, *Electrochem. Commun.*, 2021, **124**, 106938.
- 9 J. Zhang, C. Bai, Z. Wang, X. Liu, X. Li and X. Cui, *Micromachines*, 2023, **14**, mi14010155.
- 10 X. Li, J. Li, T. Wang, S. A. Khan, Z. Yuan, Y. Yin and H. Zhang, *ACS Appl. Mater. Interfaces*, 2022, **14**, 48743–48751.
- 11 C. Tian, C. Bai, T. Wang, Z. Yan, Z. Zhang, K. Zhuo and H. Zhang, *Nano Energy*, 2023, **106**, 108077.
- 12 L. Liu, D. Zhang, P. Bai, Y. Mao, Q. Li, J. Guo, Y. Fang and R. Ma, *Adv. Mater.*, 2023, **35**, 2300696.
- 13 C. Xu, Y. Sun, J. Zhang, W. Xu and H. Tian, *Adv. Energy Mater.*, 2022, **12**, 2201542.
- 14 J. T. Hupp and M. J. Weaver, *Inorg. Chem.*, 1984, **23**, 47907.
- 15 M. A. Trosheva, M. A. Buckingham and L. Aldous, *Chem. Sci.*, 2022, **13**, 4984–4998.
- 16 N. F. Antariksa, T. Yamada and N. Kimizuka, *Sci. Rep.*, 2021, **11**, 11929.
- 17 R. Hu, B. A. Cola, N. Haram, J. N. Barisci, S. Lee, S. Stoughton, G. Wallace, C. Too, M. Thomas, A. Gestos, M. E. Dela Cruz, J. P. Ferraris, A. A. Zakhidov and R. H. Baughman, *Nano Lett.*, 2010, **10**, 838–846.
- 18 A. Taheri, D. R. MacFarlane, C. Pozo-Gonzalo and J. M. Pringle, *Aust. J. Chem.*, 2019, **72**, 709–716.
- 19 M. A. Lazar, D. Al-Masri, D. R. Macfarlane and J. M. Pringle, *Phys. Chem. Chem. Phys.*, 2016, **18**, 1404–1410.
- 20 Y. Chen, Q. Huang, T. H. Liu, X. Qian and R. Yang, *EcoMat*, 2023, **5**, e12385.
- 21 Y. Liu, Q. Zhang, G. O. Odunmbaku, Y. He, Y. Zheng, S. Chen, Y. Zhou, J. Li, M. Li and K. Sun, *J. Mater. Chem. A*, 2022, **10**, 19690–19698.
- 22 M. A. Buckingham, F. Marken and L. Aldous, *Sustainable Energy Fuels*, 2018, **2**, 2717–2726.
- 23 K. Kim, S. Hwang and H. Lee, *Electrochim. Acta*, 2020, **335**, 135651.
- 24 B. Uno, N. Okumura, M. Goto and K. Kano, *J. Org. Chem.*, 2000, **65**, 1448–1455.
- 25 J. Duan, G. Feng, B. Yu, J. Li, M. Chen, P. Yang, J. Feng, K. Liu and J. Zhou, *Nat. Commun.*, 2018, **9**, 5146.
- 26 M. A. Buckingham, S. Hammoud, H. Li, C. J. Beale, J. T. Sengel and L. Aldous, *Sustainable Energy Fuels*, 2020, **4**, 3388–3399.
- 27 L. Zhang, T. Kim, N. Li, T. J. Kang, J. Chen, J. M. Pringle, M. Zhang, A. H. Kazim, S. Fang, C. Haines, D. Al-Masri, B. A. Cola, J. M. Razal, J. Di, S. Beirne, D. R. MacFarlane, A. Gonzalez-Martin, S. Mathew, Y. H. Kim, G. Wallace and R. H. Baughman, *Adv. Mater.*, 2017, **29**, 1605652.
- 28 T. Kim, J. S. Lee, G. Lee, H. Yoon, J. Yoon, T. J. Kang and Y. H. Kim, *Nano Energy*, 2017, **31**, 160–167.
- 29 H. Wang, X. Zhuang, W. Xie, H. Jin, R. Liu, B. Yu, J. Duan, L. Huang and J. Zhou, *Cell Rep. Phys. Sci.*, 2022, **3**, 100737.



- 30 H. Inoue, Y. Liang, T. Yamada and N. Kimizuka, *Chem. Commun.*, 2020, **56**, 7013–7016.
- 31 B. Yu, J. Duan, H. Cong, W. Xie, R. Liu, X. Zhuang, H. Wang, B. Qi, M. Xu, Z. L. Wang and J. Zhou, *Science*, 2020, **370**, 342–346.
- 32 L. Jiang, K. Kirihaara, V. Nandal, K. Seki, M. Mukaida, S. Horike and Q. Wei, *ACS Appl. Mater. Interfaces*, 2022, **14**, 22921–22928.
- 33 L. Jiang, S. Horike, M. Mukaida, K. Kirihaara, K. Seki and Q. Wei, *Global Chall.*, 2023, **7**, 2200207.
- 34 M. A. L. Marques, C. A. Ullrich, F. Nogueira, A. Rubio, K. Burke and E. K. U. Gross, *Time-Dependent Density Functional Theory*, Springer-Verlag, Berlin: Heidelberg, Germany, 2006.
- 35 C. Lee, W. Yang and R. G. Parr, *Phys. Rev. B: Condens. Matter Mater. Phys.*, 1988, **37**, 785–789.
- 36 B. Miehlich, A. Savin, H. Stoll and H. Preuss, *Chem. Phys. Lett.*, 1989, **157**, 200–206.
- 37 A. D. Becke, *J. Chem. Phys.*, 1993, **98**, 5648–5652.
- 38 T. H. Dunning, *J. Chem. Phys.*, 1989, **90**, 1007–1023.
- 39 D. E. Woon and T. H. Dunning, *J. Chem. Phys.*, 1993, **98**, 1358–1371.
- 40 B. Uno, N. Okumura and K. Seto, *J. Phys. Chem. A*, 2000, **104**, 3064–3072.
- 41 N. Gupta and H. Linschitz, *J. Am. Chem. Soc.*, 1997, **119**, 6384–6391.
- 42 M. Gómez, F. J. González and I. González, *J. Electrochem. Soc.*, 2003, **150**, E527.
- 43 M. Gómez, F. J. González and I. González, *Electroanalysis*, 2003, **15**, 635–645.
- 44 M. Quan, D. Sanchez, M. F. Wasylkiw and D. K. Smith, *J. Am. Chem. Soc.*, 2007, **129**, 12847–12856.
- 45 M. E. Tessensohn and R. D. Webster, *Electrochem. Commun.*, 2016, **62**, 38–43.
- 46 M. Gómez, C. Z. Gómez-Castro, I. I. Padilla-Martínez, F. J. Martínez-Martínez and F. J. González, *J. Electroanal. Chem.*, 2004, **567**, 269–276.
- 47 H. Zhou, T. Yamada and N. Kimizuka, *J. Am. Chem. Soc.*, 2016, **138**, 10502–10507.
- 48 Y. Liang, T. Yamada, H. Zhou and N. Kimizuka, *Chem. Sci.*, 2019, **10**, 773–780.
- 49 Y. Liang, J. Ka-Ho Hui, M. A. Morikawa, H. Inoue, T. Yamada and N. Kimizuka, *ACS Appl. Energy Mater.*, 2021, **4**, 5326–5331.
- 50 B. Huang, S. Muy, S. Feng, Y. Katayama, Y. C. Lu, G. Chen and Y. Shao-Horn, *Phys. Chem. Chem. Phys.*, 2018, **20**, 15680–15686.

